ACS NANO

www.acsnano.org

Chemiresistive Hydrogen Sensing with Size-Limited Palladium Nanoparticles in Iptycene-Containing Poly(arylene ether)s

Shao-Xiong Lennon Luo, Weize Yuan, Mantian Xue, Haosheng Feng, Máté J. Bezdek, Tomás Palacios, and Timothy M. Swager*

Cite This: *ACS Nano* 2023, 17, 2679−2688 | Read Online

ACCESS | Metrics & More | Article Recommendations | Supporting Information

ABSTRACT: **Metal nanoparticles have been widely employed in chemical sensing due to their high reactivity toward various gases. The size of the metal nanoparticles often dictates their reactivity and hence their performance as chemiresistive sensors. Herein, we report that iptycene-containing poly(arylene ether)s (PAEs) have been shown to limit the growth of palladium nanoparticles (Pd NPs) and stabilize the Pd NPs dispersion. These porous PAEs also facilitate the efficient transport of analytes. Single-walled carbon nanotube (SWCNT)-based chemiresistors and graphene field-effect transistors (GFETs) using these PAE-supported small Pd NPs are sensitive, selective, and robust sensory materials for hydrogen gas under ambient conditions. Generalizable strategies including presorting SWCNTs with pentiptycene-containing poly(*p*-phenylene ethynylene)s (PPEs) and thermal annealing demonstrated significant improvements in the chemiresistive performance. The polymer:NP colloids produced in this study are readily synthesized and solution processable, and these methods are of general utility.**

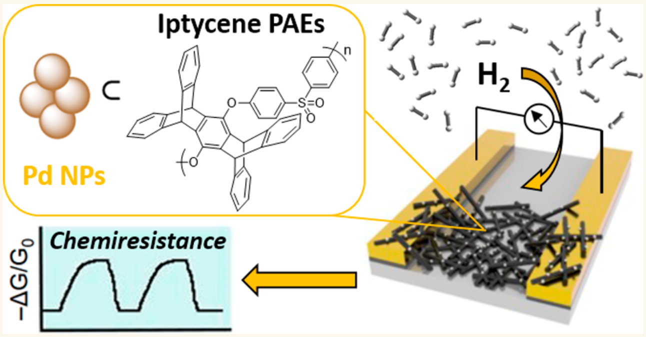

KEYWORDS: *hydrogen, gas sensing, palladium nanoparticles, carbon nanomaterials, porous polymers*

INTRODUCTION

Hydrogen gas (H_2) is abundant, widely used in many important industrial processes,[1] and represents an attractive element in renewable energy schemes.[2−4] However, there is a significant safety risk as H_2 is highly flammable and can explode when its concentration in air exceeds 4%.[5] Moreover, its buoyant, colorless, and odorless nature makes H_2 a challenging gas to detect. Therefore, it is imperative to develop sensitive and selective H_2 sensors that operate under ambient conditions for leak detection during production, transportation, storage, or usage. Current H_2 detection methods include optical, mechanical, electrochemical, and chemiresistive methods.[5−10] The ideal sensor should have miniaturized form factors and low power requirement to allow easy distributed on-site deployment and persistent monitoring.[11] Chemiresistive H_2 sensors are attractive and have been extensively studied,[9,10,12−15] as only simple electrical readouts are required to enable the continuous and real-time monitoring of H_2 concentrations. The state-of-the-art H_2 sensors include Pd-based materials,[16−18] wherein the selective absorption and reaction with H_2 creates a change in the work function and resistivity of this metal.[9,10] To achieve high sensitivity, nanoscopic highly reactive Pd structures are needed.[19] A challenge is that high surface area materials are thermodynamically unstable with regard to Ostwald ripening, which creates larger structures.[20−22] We have previously demonstrated that porous triptycene-containing poly(arylene ether) (PAE) thin films restrict the growth of silver,[23] gold,[24] and bimetallic palladium−platinum nanoparticles.[25] The PAEs have small pores that limit the growth of the metal nanoparticles during the *in situ* reduction process, where the favorable polymer−metal nanoparticles interactions help to suppress the Ostwald ripening process. However, growing metal nanoparticles on surfaces limits rapid device prototyping, batch processing, and scaled up fabrication of the sensors. In this study, we synthesize

Received: October 27, 2022
Accepted: January 9, 2023
Published: January 13, 2023

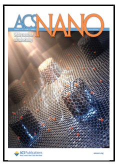

controlled small Pd NPs in colloidal dispersions that permits processability and scalability to allow for drop-casting and compatibility with inkjet printing for mass production. These PAE-supported Pd NPs were used to functionalize single-walled carbon nanotubes (SWCNTs) chemiresistors and graphene field-effect transistors (GFETs) to achieve the sensitive, selective, and robust detection of H_2 under ambient conditions.

RESULTS AND DISCUSSION

Scheme 1. Chemical Structure of Iptycene-Containing PAEs

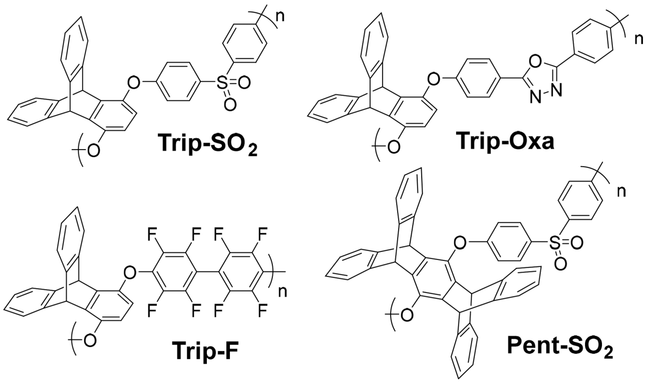

Scheme 2. Representative Synthesis of Pd NPs Supported by Iptycene-Containing PAEs

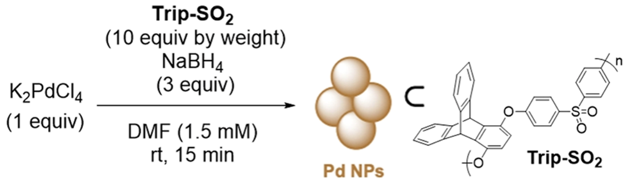

Following a modified procedure,[26] we have synthesized iptycene-containing PAEs via a microwave-assisted S_NAr polycondensation reaction between triptycene-1,4-diol/pentiptycene-6,13-diol and the respective fluoro-containing partners, yielding PAEs **Trip-SO$_2$**, **Trip-Oxa**, **Trip-F**, and **Pent-SO$_2$** (Scheme 1). The resulting polymers were characterized by gel permeation chromatography (GPC) and nuclear magnetic resonance (NMR) (Supporting Information, Figures S19−S22). The iptycene-containing PAEs were dissolved together with K_2PdCl_4 in DMF, and Pd NPs are generated by subsequent $NaBH_4$ reduction (Scheme 2). Upon the addition of $NaBH_4$ solution, the reaction mixture instantaneously turned reddish brown, indicating the formation of a Pd NP dispersion. To examine the effect of PAEs on the Pd nanoparticle growth, the resulting Pd NP dispersions were characterized by transmission electron microscopy (TEM). As shown in Figure S1, Pd NPs synthesized in the presence of **Trip-SO$_2$** (**Trip-SO$_2$-Pd**) have significantly smaller diameters (3−5 nm) than the control Pd NPs in the absence of PAE (>200 nm). It should be noted that **Trip-SO$_2$-Pd** is observed to be homogeneous and well-dispersed across large areas (Figure S1). The **Trip-SO$_2$-Pd** dispersion also possesses high stability and stays in solution after weeks of storage. To confirm the chemical identity of the nanoparticles, we performed energy-dispersive X-ray (EDX) elemental mapping on **Trip-SO$_2$-Pd** and the Pd peaks correlate to the NP images (Figure S2). Similarly, as shown in Figure 1, other iptycene-containing PAEs also yielded small Pd NPs where the majority of the Pd NP diameter falls under 5 nm (Figure S3). To highlight the importance of the iptycene units in supporting the size-limited Pd NPs, we have also performed the Pd NPs synthesis with the common poly(ether ether sulfone) (**PEES**) that does not contain iptycene moieties. In this case, the Pd NPs rapidly aggregated and phase-separated as shown in Figure S4. Collectively, we have demonstrated iptycene-containing PAEs in the synthesis of stable size-limited Pd NP dispersions.

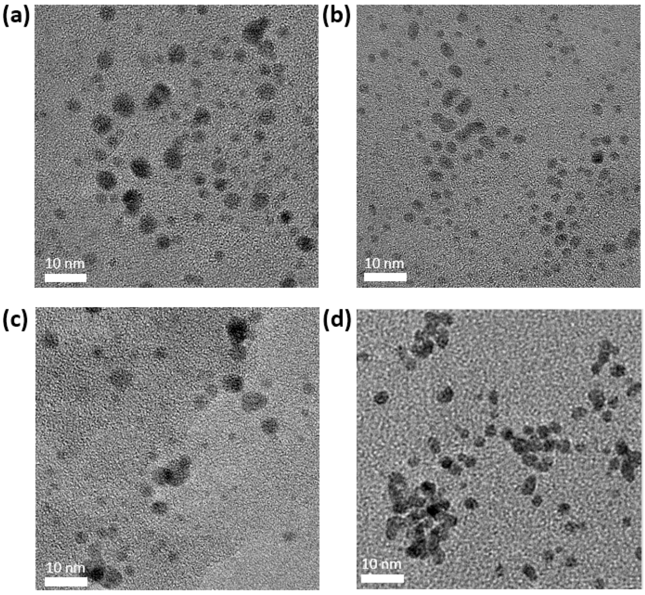

Figure 1. TEM images of (a) Trip-SO$_2$-Pd, (b) Trip-Oxa-Pd, (c) Trip-F-Pd, and (d) Pent-SO$_2$-Pd.

To investigate the potential of these PAE-supported Pd NPs in hydrogen sensing, we fabricated chemiresistive SWCNT-based devices[27−30] as illustrated in Figure S5. In this process, SWCNTs are dispersed and drop-casted over gold electrode arrays to form a conductive network. Subsequently, PAE-supported Pd NPs dispersions are drop-casted on top of this SWCNT network, serving as the selector element that interacts with the analyte and SWCNTs in the sensing device. We characterized the surface morphology of drop-cast PAE:Pd NP films with a scanning electron microscope (SEM). As shown in Figure S6, the films retain the porous structures that are expected from the parent PAEs, providing fast kinetics for analyte diffusion.[23,31] For the initial screening, the chemiresistive devices fabricated were exposed to 1% H_2 for 10 min in dry air at room temperature, and the change in resistance was converted to the negative normalized change in conductance as the sensing readout ($-\Delta G/G_0$, ΔG, and G_0 are the change in conductance and the baseline conductance, respectively). As shown in Figure 2, we observe reversible decreases in conductance upon exposure to H_2 gas and excellent tolerance to oxygen. Shaded areas represent the standard deviations in the chemiresistive responses measured, suggesting good reliability of the drop-casting fabrication method with low device-to-device variance. When compared to larger Pd NPs synthesized in the absence of PAEs (**Pd Only**), all PAE-supported Pd NPs showed significantly higher responses,

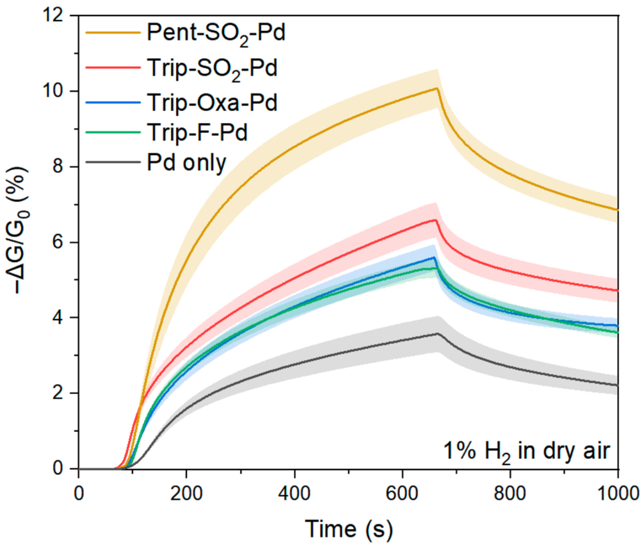

Figure 2. Chemiresistive responses of PAE-supported Pd NPs to 1% H_2 in dry air for 10 min ($N \geq 4$).

which is expected from the smaller Pd NPs. In particular, **Trip-SO$_2$-Pd** and **Trip-Oxa-Pd** were observed to respond more strongly to H_2 than **Trip−F-Pd**, possibly due to the more coordinating nature of the sulfone and oxazole groups in the polymers that could help to facilitate the sensing signal transduction. More noteworthy is that **Pent-SO$_2$-Pd** displayed the highest sensitivity toward H_2 with an averaged 10.1% change in conductance, higher than the averaged 6.6% response from its triptycene counterpart, suggesting the beneficial effect of the pentiptycene moiety in this composite sensory material. Moreover, the PAE-supported Pd NPs are compared against Pd NPs supported by commercial polyvinylpyrrolidone (PVP, M_n = 55 kDa) which has been commonly used as a capping agent in metal nanoparticle synthesis.[21,32] Pd NPs synthesized in the presence of PVP (**PVP-Pd**) displayed significantly lower response toward 1% H_2 than PAE-supported Pd NPs, even though they are found to have similar particle size distributions (Figure S7). The sensor response and recovery kinetics of **PVP-Pd** are also found to be much slower. This can be attributed to the difference in the intrinsic porosity of the polymers, where porous PAEs such as **Pent-SO$_2$** and **Trip-SO$_2$** possess significantly higher surface area as shown by BET analysis (Figure S8). SEM studies also show that **PVP-Pd** displays a nonporous surface morphology (Figure S9). There seems to be an apparent correlation between the chemiresistive response and the polymer porosity where a higher surface area could facilitate the diffusion and the interaction between gas analytes and Pd NPs more effectively, highlighting the advantage of the porous PAEs in creating a conducive environment for gas sensing.

The mechanism for chemiresistive H_2 sensing by Pd-based materials has been postulated to involve the absorption of H_2 and the formation of palladium hydrides in α- and/or β-phase that result in an increase in resistivity and a change in work function.[10] However, as the Pd NPs are scattered across the SWCNT network in our system, the change in the surface doping effect of the Pd NPs with H_2 seems more likely. Specifically, a reduction−oxidation mechanism (Scheme 3) is possible where the palladium nanoparticles oxidized in air are reduced by H_2 to Pd(0), similar to previously reported PdO-based H_2 sensors.[33−35] The reduced particles release electrons that compensate for the holes in the *p*-doped SWCNTs to produce the observed decrease in conductance.[27] When H_2 is removed from the atmosphere, Pd(0) species are reoxidized by the ambient air and give rise to the recovery of the SWCNT conductance. To test this hypothesis, **Pent-SO$_2$-Pd** was exposed to 1% H_2 under a nitrogen atmosphere. As shown in Figure 3, **Pent-SO$_2$-Pd** responded more strongly to 1% H_2 in nitrogen than in dry air (17.4% vs 10.1%), consistent with the right shift in the proposed equilibrium that favors the formation of the reduced palladium species in nitrogen. Subsequently, when H_2 gas was switched off and the sensor was allowed to rest in nitrogen, no recovery of conductance was observed. This lack of reversibility indicates that our sensor does not operate under the absorption−desorption mechanism found in other Pd-based chemiresistive H_2 sensors.[10] Moreover, this irreversible reduction process in nitrogen also resulted in a significantly smaller chemiresistive response during the second H_2 exposure. At the last stage where the carrier gas was switched back to dry air, we observed a rapid conductance increase as the sensors start to recover. This necessity of oxygen in sensor recovery again corroborates with the reduction−oxidation sensing mechanism proposed. For future development of these sensors, the sensing speed can be improved by heating to increase the rates of the redox reactions.

Scheme 3. Proposed H_2-Sensing Mechanism of PAE-Supported Pd NPs

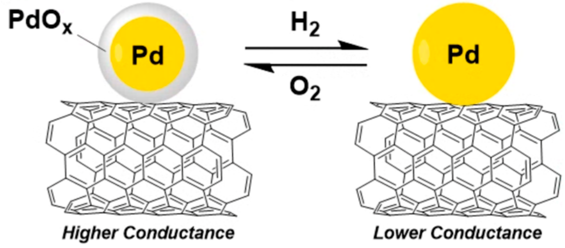

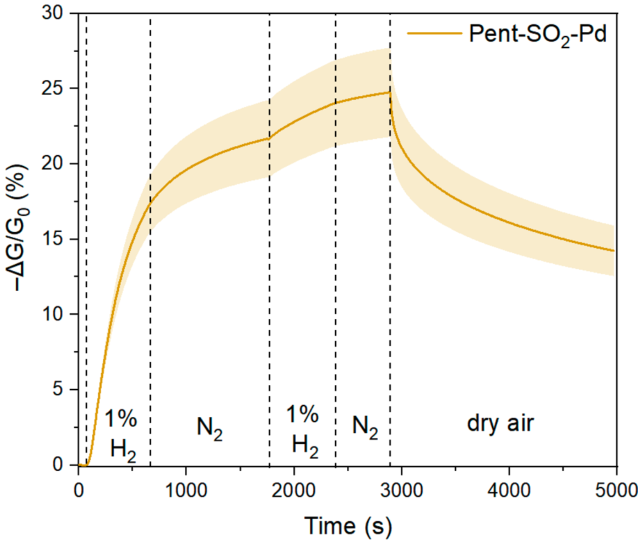

Figure 3. Chemiresistive responses of Pent-SO$_2$-Pd to 1% H_2 in nitrogen ($N \geq 4$).

In search of further evidence for the reduction process, we have also characterized the PAE-supported Pd NPs with X-ray photoelectron spectroscopy (XPS) to evaluate the oxidation states of Pd species during H_2 sensing. High-resolution XPS Pd 3d spectra of **Pent-SO_2-Pd** were investigated before and after the H_2 exposure (Figure 4). Multiple Pd peaks were observed in the fabricated **Pent-SO_2-Pd** device that can be assigned to Pd(0), PdO, and PdO_2.[36,37] Upon H_2 exposure, Pd 3d peaks of palladium oxides significantly diminished whereas Pd(0) became the predominant Pd species found in the material, suggesting the effective reduction by H_2. This observation by XPS further supports the reduction−oxidation sensing mechanism.

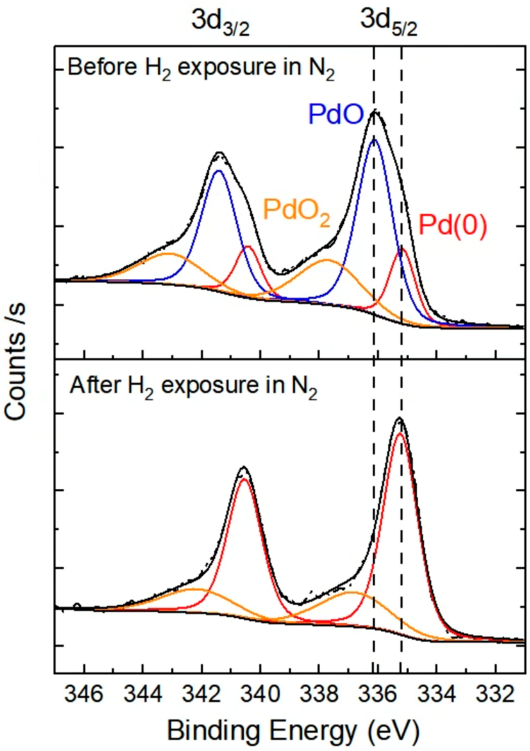

Figure 4. XPS Pd 3d region of Pent-SO_2-Pd (top) before and (bottom) after 1% H_2 exposure in nitrogen.

We have also applied the PAE-supported Pd NPs to graphene sensors based on field-effect transistors (GFETs). Single-layer graphene is highly sensitive to the surface electronic perturbation and has been used widely as the transduction material in sensing.[38−41] We fabricated an array of GFET devices (Figure S10) with low defect single-layer graphene (Figure S11) and then drop-casted **Pent-SO_2-Pd** on the surface. As shown in Figure S12, we observed a significant and reversible chemiresistive response from the GFET upon exposure to 1% H_2 in dry air, whereas the control GFET with bare graphene gave a negligible response. The electronic properties of GFETs can be readily modulated by gate potential, which can provide insight into the sensing mechanism. Figure 5 reveals the transfer characteristics of the GFETs with **Pent-SO_2-Pd** before and after the H_2 exposure. The current between source and drain (I_{ds}) was measured when the applied gate voltage (V_{gs}) swept from −6 to 6 V. A notable left shift (~1 V) of the Dirac point (minimum conduction point) in the $I-V$ curve was observed after the H_2 exposure, indicating an n-type doping effect[41,42] as a result of the interaction between the Pd NPs and H_2. This observation is consistent with the proposed reduction−oxidation sensing mechanism. Moreover, we have demonstrated that the use of PAE-supported Pd NPs can be extended to other sensing platforms where efforts are currently underway to incorporate them into highly multiplexed sensing arrays.

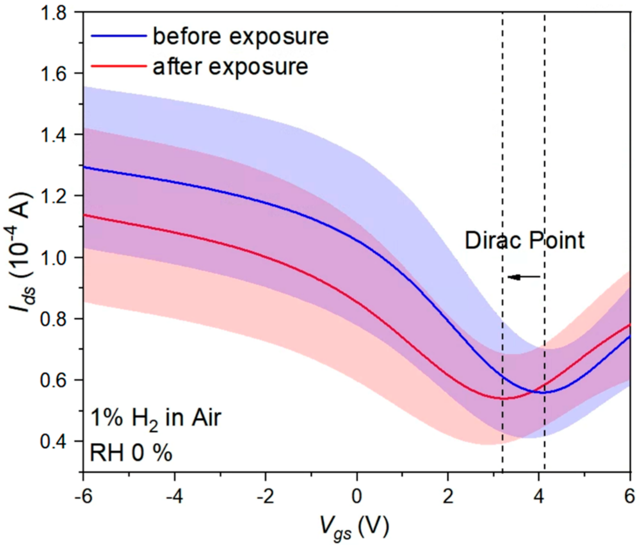

Figure 5. Transfer characteristics change of GFETs functionalized with Pent-SO_2-Pd in response to 1% H_2 in dry air for 10 min ($N \geq 16$).

The sensitivity of SWCNT-based chemiresistors highly depends on the SWCNT purity and the semiconducting content,[43] and it is desirable to purify/sort the commercial SWCNTs to improve their chemiresistive response. Our group has previously reported a diameter-selective SWCNT dispersion method using poly(p-phenylene ethynylene) s (PPEs) containing pentiptycene moieties.[44] Polymers **P1** and **P2**, as illustrated in Figure 6a, were shown to selectively disperse SWCNTs with diameters of 0.8−0.9 nm with the exclusion of amorphous carbon impurities and metallic SWCNTs with larger diameters. We used **P1** and **P2** to disperse SWCNTs and subsequently isolated the dispersed SWCNTs by centrifugation, filtration, redispersion, and washing to remove the excess polymer. The resulting purified SWCNTs are dispersed in oDCB (**P1-SWCNT** and **P2-SWCNT**) and showed interesting green and pink colors with high dispersion stability (Figure 6d, inset). The absorption spectra (Figure 6d) of **P1-SWCNT** and **P2-SWCNT** display new absorption peaks (*) that do not belong to either the pristine SWCNTs (**p-SWCNT**) or the pentiptycene polymers. These peaks likely resulted from new charge transfer between the polymer and SWCNTs. Sensing devices using the presorted **P1-SWCNT** and **P2-SWCNT** with **Pent-SO_2-Pd** showed significant improvement in the H_2 sensitivity (Figure 7). Specifically, when compared to the 10.1% conductance change achieved by **p-SWCNT/Pent-SO_2-Pd**, chemiresistive devices made from **P1-SWCNT/Pent-SO_2-Pd** and **P2-SWCNT/Pent-SO_2-Pd** showed 12.0% and 20.1% change in conductance, respectively. This trend of sensitivity is consistent with our previous study in benzene, toluene, and o-xylene (BTX) sensing where similar pentiptycene polymer/SWCNT dispersions were used as sensing elements.[44] These improvements demonstrate that polymer sorting is an effective strategy to modulate the chemiresistive sensitivity of the

https://doi.org/10.1021/acsnano.2c10736
ACS Nano 2023, 17, 2679−2688

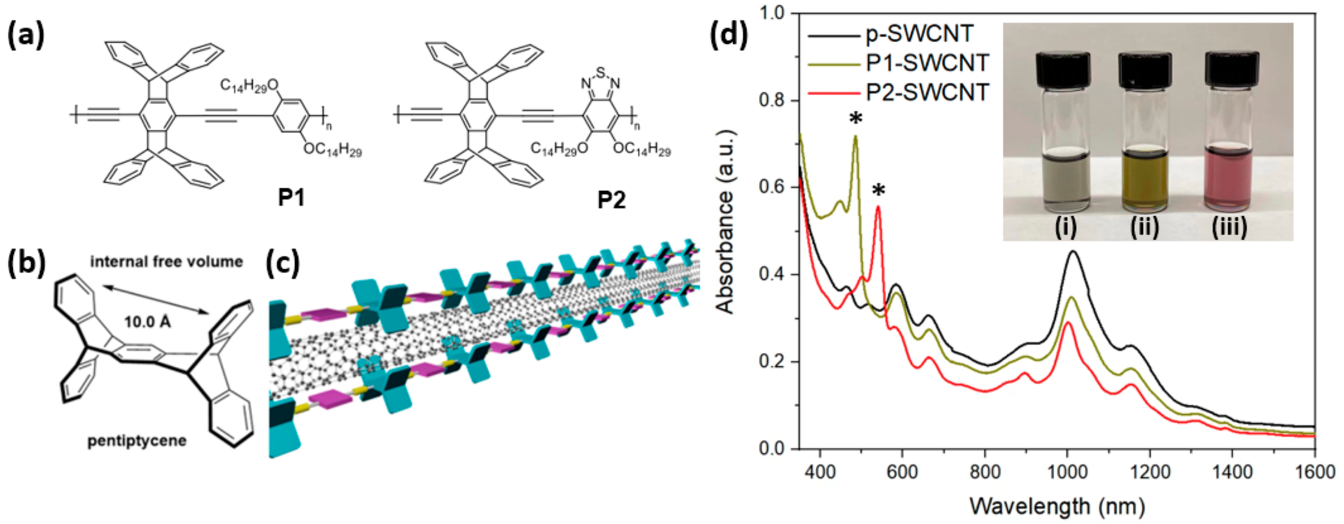

Figure 6. (a) Chemical structure of P1 and P2. (b) Structural property of pentiptycene. (c) Schematic drawing of the dispersion of SWCNTs between pentiptycene polymers. (d) UV−vis−NIR absorption spectra of pristine SWCNTs and sorted SWCNTs dispersions in *o*DCB. Inset: Photographs of dispersions of (i) p-SWCNT, (ii) P1-SWCNT, and (iii) P2-SWCNT in *o*DCB. Adapted from ref 44. Copyright 2020 American Chemical Society.

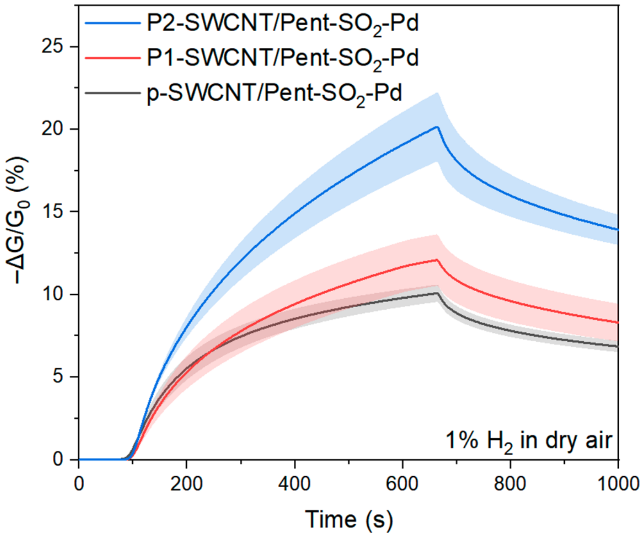

Figure 7. Chemiresistive responses of Pent-SO$_2$-Pd on various SWCNTs to 1% H_2 in dry air for 10 min ($N \geq 4$).

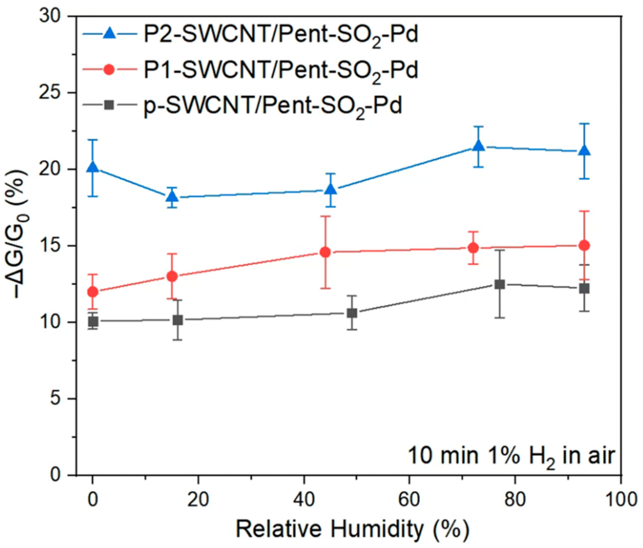

Figure 8. Summary of chemiresistive responses of Pent-SO$_2$-Pd on various SWCNTs to 1% H_2 for 10 min in different relative humidity levels ($N \geq 4$).

SWCNT-based devices by increasing the semiconducting content and the purity of the SWCNTs transducer material.

Notably, these sensors containing PAE-supported Pd NPs showed excellent tolerance to humidity, which often compromises the performance in chemiresistive H_2 sensors.[10] The **Pent-SO$_2$-Pd**-based sensors examined were able to perform well at high humidity (>90% relative humidity) and maintained a similar level of sensitivity across the relative humidity range investigated (Figure 8). This observation is in stark contrast to many reported Pd-based systems[10] and can be attributed to the PAE-supported Pd NPs preventing mechanisms wherein water interrupts the desired H_2-Pd NP reactions or the Pd NP-SWCNT interactions.

We find that thermally annealing the fabricated sensing devices produces a drastic sensitivity increase to H_2. Various SWCNTs sensing devices containing **Pent-SO$_2$-Pd** were placed in a muffle oven at 275 °C for 1 h under air. As shown in Figure 9, large improvements were observed for all the devices in response to 1% H_2. Notably, thermally annealed **P2-SWCNT/Pent-SO$_2$-Pd** displayed a significant 18-fold increase in sensitivity (362% change in conductance), making it comparable to the most sensitive Pd-based chemiresistive sensors in response to 1% H_2 under ambient conditions (Figure S13). A shorter annealing time (15 min) was attempted (Figure S14), and a 2-fold increase in H_2 sensitivity was observed. Consistent with the reduction and oxidation of the Pd species, thermally annealing the Pd NPs at an elevated temperature could produce a larger amount of Pd oxides, which would result in a larger change with the subsequent H_2 reduction. To verify this hypothesis, the high-resolution XPS of the Pd 3d region was performed on the thermally annealed Pd NPs, showing most of the Pd(0) converted to PdO species (Figure S15−S16). Also, we observed a significant decrease in the baseline conductance, which can be attributed to the oxidation of SWCNTs during the thermal annealing process.

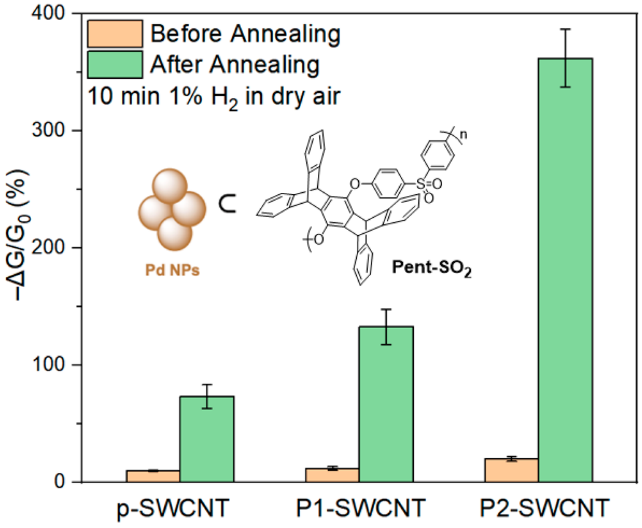

Figure 9. Comparison of chemiresistive responses of Pent-SO_2-Pd on various SWCNTs to 1% H_2 in dry air for 10 min before and after the thermal annealing process ($N \geq 4$).

To evaluate if changes in the SWCNTs occurred, we have characterized the thermally annealed samples by Raman spectroscopy. A significant increase in the D-band/G-band ratio, which is an indicator for surface defect density,[45] was observed after the thermal annealing process (Figure S17). The oxygen defect sites introduced on the SWCNT surface may lead to the direct binding of the Pd NPs, which facilitates the changes in charge transfer that are the basis of the transduction mechanism.[46,47] The improvement in H_2 sensitivity after thermal annealing may be the result of both Pd NPs oxidation and SWCNTs modification.

The range of concentrations over which a sensor accurately operates is of general interest. As shown in Figure 10, thermally annealed **P2-SWCNT/Pent-SO_2-Pd** was tested under a wide range of H_2 concentrations from 100 ppm to 1% (10,000 ppm). In the high H_2 concentration regime, thermally annealed **P2-SWCNT/Pent-SO_2-Pd** displayed plateau responses during the end of the H_2 exposure, showing signs of sensor saturation. On the other hand, when H_2 was at low ppm levels, no significant saturation was observed in the sensing traces. Notably, a 3.2% conductance change was observed in response to 100 ppm of H_2. The sensor saturation at high concentrations is revealed by the nonlinearity in Figure 10c. However, the responses to H_2 at ppm levels display a linear correlation (Figure 10d) to allow accurate quantification of the H_2 concentration. The limit of detection (LOD) is calculated to be 91 ppm from the linear fit. It should be noted that this LOD is far below the sensitivity requirement of 1000 ppm outlined by the United States Department of Energy (DOE).[48] As illustrated in Figure 10b, the sensors did not show signs of saturation after the 10 min exposure at low H_2 concentrations, suggesting their potential to achieve a much lower LOD with a longer exposure time.

We examined the selectivity of the sensors through exposure to potential interfering analytes. Thermally annealed **P2-SWCNT/Pent-SO_2-Pd** was exposed to a wide variety of common volatile organic compounds (VOCs) and gases such as methane and carbon monoxide. As shown in Figure 11, at a concentration of 500 ppm, thermally annealed **P2-SWCNT/Pent-SO_2-Pd** displayed 1 order of magnitude higher responses toward H_2 than other interferents, highlighting its excellent selectivity. We have also evaluated the humidity effect on the H_2 sensing for thermally annealed **P2-SWCNT/Pent-SO_2-Pd**. As shown in Figure S18, the response toward 1% H_2 is largely maintained until high humidity (>60% relative humidity). The higher sensitivity to humidity reflects the more hydrophilic character of the PdO-rich NPs and functionalized SWCNTs after the thermal annealing process. Humidity effects can be mitigated by adding a drying element in the sensing setup to allow for practical sensor deployment in most scenarios.

CONCLUSION

We have reported the synthesis of colloidal size-limited Pd NPs with iptycene-containing PAEs and used them to create sensitive, selective, and robust chemiresistive hydrogen sensors. Rather than the common absorption−desorption sensing mechanism, a reduction−oxidation mechanism was found to be operative in this SWCNT-based construct and reversible H_2 sensing responses are achieved in ambient air. Moreover, these size-limited PAE-supported Pd NPs can be used to create GFET sensors that were also used to elucidate the sensing mechanism. The excellent humidity tolerance may be attributed to the PAE groups and will be explored to see if it has general utility in chemiresistive sensors. Presorting of SWCNTs by complexation to pentiptycene polymers and thermal annealing enhance the sensor performance, which can be generalized to guide future sensor design.

MATERIALS AND METHODS

Materials. Commercial reagents were purchased from Sigma-Aldrich, Alfa Aesar, Combi-Blocks, Oakwood, and Ambeed and used as received unless otherwise noted. Deuterated solvents were purchased from Cambridge Isotope Laboratories and used as received. Single-walled carbon nanotubes [Signis SG65i, lot no.: MKBZ1159 V; (6,5) chirality, ≥93% carbon as SWCNT; 0.7−0.9 nm diameter] were purchased from Sigma-Aldrich and used as received. Hydrogen, methane, and carbon monoxide gas cylinders were purchased from Airgas. TEM grid (Carbon Type-B, 300 mesh, Copper) was purchased from Ted Pella. Triptycene-1,4-diol, pentiptycene-6,13-diol, **P1**, and **P2** are synthesized according to procedures in the literature.[44,49,50]

Instruments. NMR spectra were recorded using a Bruker Avance 500 MHz NMR spectrometer. Polymer samples were analyzed in THF using an Agilent 1260 Infinity GPC system with a variable wavelength diode array (254, 450, and 530 nm) and refractive index detectors. The instrument was calibrated with narrow-dispersity polystyrene standards between 1.7 and 3150 kg mol^{-1}. Polymer samples were also analyzed in 25 mM LiBr DMF using an Agilent 1260 Infinity setup with two Shodex KD-806 M columns in tandem. The differential refractive index (dRI) was monitored using a Wyatt Optilab T-rEX detector. The light scattering was monitored using a Wyatt DWAN HELEOS-II detector. Tip sonication was performed with Qsonica Q125 Sonicator. Microwave-assisted reactions were performed with a CEM Discover 2.0 Microwave Synthesizer. Brunauer−Emmett−Teller (BET) surface areas of polymers were measured with N_2 sorption at 77 K using a Micromeritics ASAP 2020. Raman spectra were collected using a Horiba Jobin-Yvon LabRam (Model HR 800) Raman confocal microscope with a 633 nm laser. X-ray photoelectron spectroscopy (XPS) measurements were performed on a Thermo Scientific K-Alpha+ X-ray photoelectron spectrometer. TEM characterization and EDX mapping were performed via a 120 kV FEI Tecnai Multipurpose Digital TEM (G2 Spirit TWIN). SEM characterization was conducted with a Merlin and Crossbeam 540 Zeiss. Absorption spectra were obtained using an Agilent Cary 4000 UV−vis−NIR spectrophotometer. Mass flow controllers (MFCs) were purchased from Alicat Scientific, with carrier gas flow rates (air

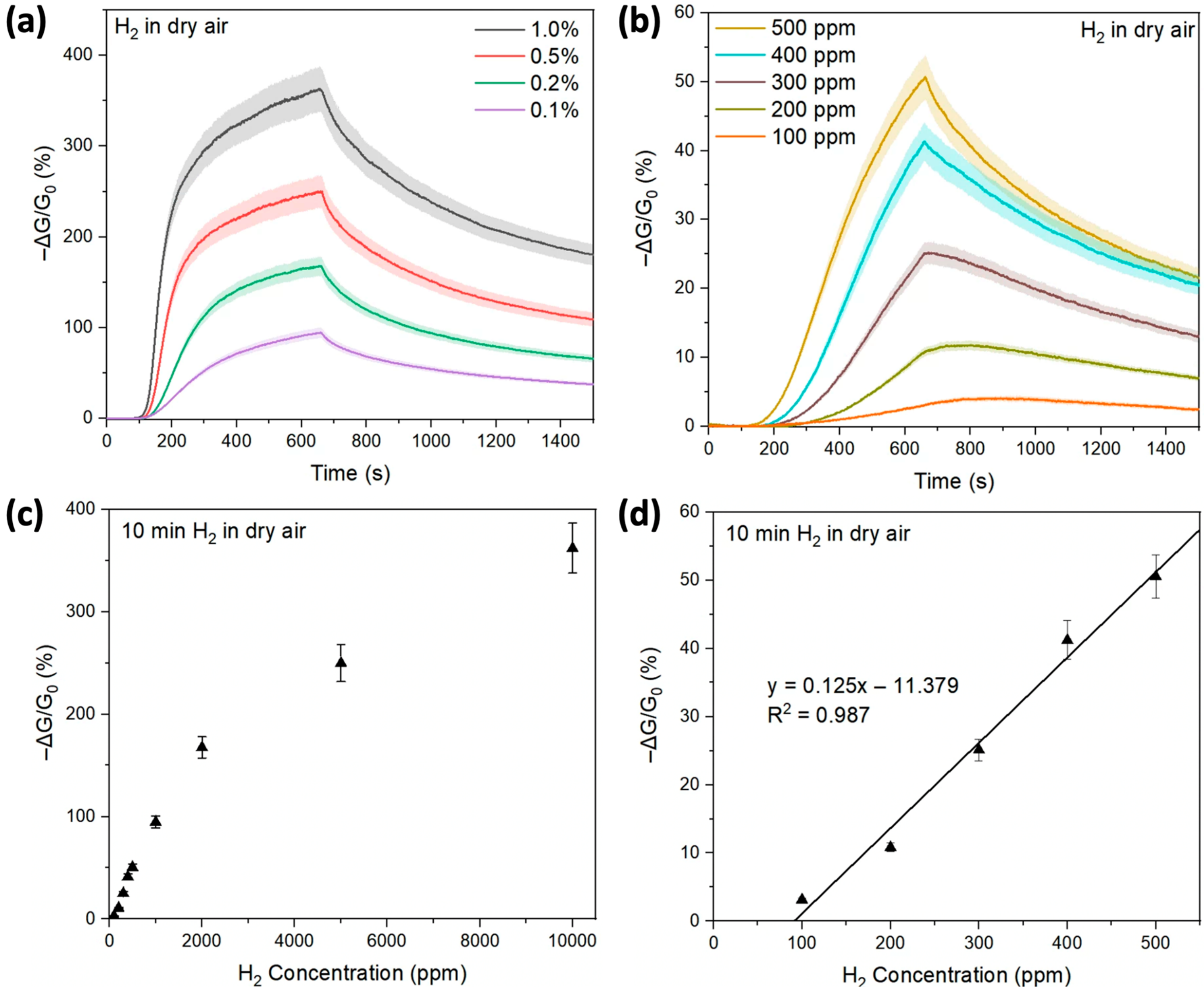

Figure 10. (a,b) Chemiresistive responses of thermally annealed P2-SWCNT/Pent-SO$_2$-Pd to different concentrations of H$_2$ in dry air. (c) Summary of chemiresistive responses of thermally annealed P2-SWCNT/Pent-SO$_2$-Pd to different concentrations of H$_2$ in dry air. (d) Calibration curve of thermally annealed P2-SWCNT/Pent-SO$_2$-Pd to 100−500 ppm of H$_2$ in dry air for 10 min ($N \geq 4$).

or nitrogen) controlled using an MC-10 SLPM-D/5 M and hydrogen flow rates controlled using an MC-10SCCM-D/5M. Analyte gases were generated by a FlexStream FlexBase module. Resistance was measured using an Agilent Keysight 34970A equipped with a 34901A 20-channel multiplexer module. The scan rate was set to 1 scan/second.

Synthesis of Trip-SO$_2$. A 5 mL microwave vial was charged with a magnetic stir bar, triptycene-1,4-diol (0.20 mmol), and bis(4-fluorophenyl) sulfone (1 equiv). Two milliliters of anhydrous *N*,*N*-dimethylacetamide (DMAc) was added, the reaction mixture for sparged with nitrogen for 15 min, and K$_2$CO$_3$ (2 equiv) was added. The reaction mixture was heated to 200 °C for 1 h under microwave irradiation. After the reaction mixture was cooled to room temperature, it was precipitated in methanol. The white precipitates were filtered, washed with water, and dried *in vacuo*. GPC (THF): M_n = 1.6× 10^4 Da, PDI = 1.4.

Synthesis of Trip-Oxa. A 5 mL microwave vial was charged with a magnetic stir bar, triptycene-1,4-diol (0.20 mmol), and 2,5-bis(4-fluorophenyl)-1,3,4-oxadiazole (1 equiv). Two milliliters of anhydrous *N*,*N*-dimethylacetamide (DMAc) was added, the reaction mixture was sparged with nitrogen for 15 min, and K$_2$CO$_3$ (2 equiv) was added. The reaction mixture was heated to 200 °C for 1 h under microwave irradiation. After the reaction mixture was cooled to room temperature, it was precipitated in methanol. The white precipitates were filtered, washed with water, and dried *in vacuo*. GPC (THF): M_n = 2.0 × 10^4 Da, PDI = 1.6.

Synthesis of Trip-F. A 5 mL microwave vial was charged with a magnetic stir bar, triptycene-1,4-diol (0.20 mmol), and decafluorobiphenyl (1 equiv). Two milliliters of anhydrous *N*,*N*-dimethylacetamide (DMAc) was added, the reaction mixture was sparged with nitrogen for 15 min, and K$_2$CO$_3$ (2 equiv) was added. The reaction mixture was heated to 180 °C for 1 h under microwave irradiation. After the reaction mixture was cooled to room temperature, it was precipitated in methanol. The white precipitates were filtered and washed with water and dried *in vacuo*. GPC (THF): M_n = 1.0 × 10^4 Da, PDI = 1.9.

Synthesis of Pent-SO$_2$. A 5 mL microwave vial was charged with a magnetic stir bar, pentiptycene-6,13-diol (0.20 mmol), and bis(4-fluorophenyl) sulfone (1.05 equiv). Two milliliters of anhydrous *N*,*N*-dimethylacetamide (DMAc) was added, the reaction mixture was sparged with nitrogen for 15 min, and K$_2$CO$_3$ (2 equiv) was added. The reaction mixture was heated to 180 °C for 1 h under microwave irradiation. After the reaction mixture was cooled to room temperature, it was precipitated in methanol. The white precipitates were filtered, washed with water, and dried *in vacuo*. GPC (DMF, soluble fraction): M_n = 4.2 × 10^4 Da, PDI = 1.8.

General Procedure for the Synthesis of Palladium Nanoparticles with Poly(arylene ether)s (PAEs). A 20 mL scintillation

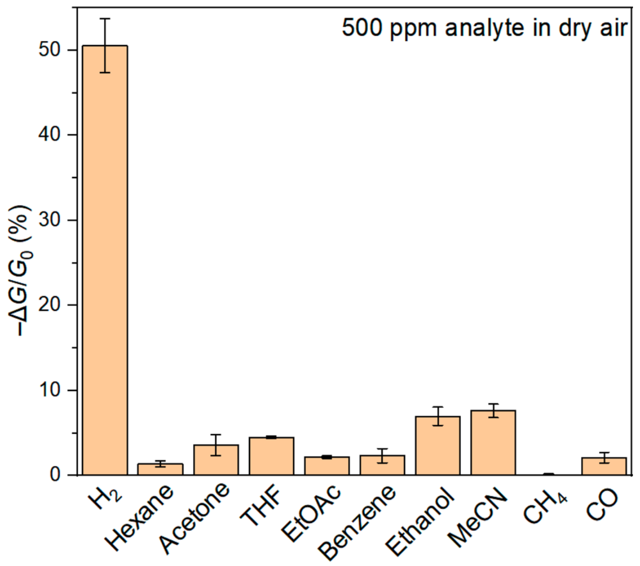

Figure 11. Summary of chemiresistive responses of thermally annealed P2-SWCNT/Pent-SO_2-Pd in response to different volatile organic vapors and gases. Devices were exposed to analyte at 500 ppm in dry air for 10 min ($N \geq 4$).

vial was charged with a magnetic stirbar. PAE (10 mg), K_2PdCl_4 (1.0 mg), and 2 mL of anhydrous *N*,*N*-dimethylformamide (DMF) were added and sonicated to dissolve the materials. Subsequently, 5 μL of a solution of $NaBH_4$ in anhydrous DMF (70 mg of $NaBH_4$ in 1 mL of DMF) was added, and the solution was stirred at room temperature for 15 min.

Preparation of SWCNT Dispersion. For pristine SG65i SWCNTs, a stock solution of SG65i SWCNTs (2 mg) was prepared in *o*-dichlorobenzene (*o*DCB) (20 mL) by bath sonication at rt for 30 min. Subsequently, the suspension was allowed to stand overnight undisturbed. For polymer/SWCNT dispersions, polymer (2 mg) was dissolved in *o*-dichlorobenzene (*o*DCB, 2 mL), and the solution was sonicated in a water bath for 10 min. To the polymer solution was added 0.2 mg of SG65i SWCNTs, and the resulting mixture was chilled with ice and homogenized for 20 min using a Qsonica Q125 sonicator at 63W with a pulse sequence (10 s ON and 5 s OFF). Subsequently, the suspension was centrifuged for 3 h at 22000*g*. The supernatant was removed, filtered, dispersed in *o*DCB, filtered, and washed with copious amounts of chloroform, tetrahydrofuran (THF), and acetone. The resulting SWCNT film was redispersed in *o*DCB (10 mL) to yield the final polymer/SWCNT dispersion.

Chemiresistive Device Preparation. Glass slides (VWR microscope slides) were bath sonicated in acetone for 15 min and then dried with a stream of nitrogen. Using an aluminum mask, chromium (15 nm) followed by gold (50 nm) was deposited using a thermal evaporator (Angstrom Engineering), leaving a 0.5 mm gap between gold electrodes. A 1 μL amount of the SWCNT dispersion was drop-casted in between the gold electrodes and dried at rt under house vacuum in a desiccator or vacuum oven. Subsequently, a 1 μL amount of the PAE-supported Pd NPs dispersion was drop-casted in between the gold electrodes and dried at rt. Finally, the fabricated sensor device was soaked in Milli-Q water for 1 h to remove residual $NaBH_4$ and dried at rt under house vacuum in a desiccator or vacuum oven.

Graphene Field Effect Transistor (GFETs) Preparation. Fabrication of the GFETs started with a piranha cleaned 4-in. silicon wafer. 5 nm Ti and 100 nm Au were deposited as gate electrodes using electron beam deposition. Twenty nanometers of aluminum oxide film was deposited using atomic layer deposition (ALD). Another two layers of metal stacks (Ti/Au) were deposited to form the source and drain contacts of the sensor array. Twenty nanometers of aluminum oxide as the interlayer dielectric was deposited using ALD. BCl_3 plasma was used to etch openings on the oxide film. Wafer was then diced into chips. Graphene coated with poly(methyl methacrylate) (PMMA) (ACS Materials Trivial Transfer Graphene 1 cm × 1 cm) was transferred on the chip to cover the sensing area. The chip was baked at 60 °C for 30 min and 130 °C for 15 min. The chip was immersed in acetone overnight to remove the PMMA film. The graphene film was isolated into individual channels with oxygen plasma and a patterned PMGI/AZ3312 resist stack as a mask. The chip was then immersed in *N*-methyl-2-pyrrolidone (NMP) for several hours to strip away the resist. The sensing chip was passivated with 500 nm of patterned SU8 film, where only the graphene channel is exposed to functionalization and analytes. The sensing chip was cleaned with IPA and blow dried with a nitrogen gun. Finally, a 1 μL amount of the PAE-supported Pd NPs dispersion was drop-casted on the GFETs and dried at rt under house vacuum in a desiccator.

Graphene Field Effect Transistor (GFET) Measurement. All electrical measurements were performed using a custom-built measurement system[42] at room temperature. For *I*−*V* sweep measurements, the drain-source voltage V_{ds} was held constant and the gate-source voltage V_{gs} was swept from −6 to 6 V in 50 mV increments. A 10 s hold time was used before the gate-source voltage V_{gs} was swept at a rate of 50 mV/500 ms. For chemiresistive measurement, V_{gs} was zero and V_{gs} was held constant at 500 mV. The current of the graphene channel was sampled every 500 ms.

Thermal Annealing of the Sensor Device. The fabricated sensor devices were placed in a muffle oven at 275 °C for 1 h under ambient air, followed by cooling to room temperature.

ASSOCIATED CONTENT

Supporting Information

The Supporting Information is available free of charge at https://pubs.acs.org/doi/10.1021/acsnano.2c10736.

Additional sensing and characterization data (TEM, SEM, XPS, Raman, NMR, BET surface area) (PDF)

AUTHOR INFORMATION

Corresponding Author

Timothy M. Swager − *Department of Chemistry and Institute for Soldier Nanotechnologies, Massachusetts Institute of Technology, Cambridge, Massachusetts 02139, United States*; orcid.org/0000-0002-3577-0510;
Email: tswager@mit.edu

Authors

Shao-Xiong Lennon Luo − *Department of Chemistry and Institute for Soldier Nanotechnologies, Massachusetts Institute of Technology, Cambridge, Massachusetts 02139, United States*; orcid.org/0000-0001-5308-4576
Weize Yuan − *Department of Chemistry and Institute for Soldier Nanotechnologies, Massachusetts Institute of Technology, Cambridge, Massachusetts 02139, United States*
Mantian Xue − *Department of Electrical Engineering & Computer Science, Massachusetts Institute of Technology, Cambridge, Massachusetts 02139, United States*
Haosheng Feng − *Department of Chemistry and Institute for Soldier Nanotechnologies, Massachusetts Institute of Technology, Cambridge, Massachusetts 02139, United States*; orcid.org/0000-0003-1031-7733
Máté J. Bezdek − *Department of Chemistry and Institute for Soldier Nanotechnologies, Massachusetts Institute of Technology, Cambridge, Massachusetts 02139, United States*; orcid.org/0000-0001-7860-2894
Tomás Palacios − *Department of Electrical Engineering & Computer Science, Massachusetts Institute of Technology, Cambridge, Massachusetts 02139, United States*

Complete contact information is available at:
https://pubs.acs.org/10.1021/acsnano.2c10736

Notes

The authors declare no competing financial interest.

ACKNOWLEDGMENTS

The authors gratefully acknowledge Eni S.p.A. for funding this research through the MIT Energy Initiative and the National Science Foundation (DMR-2207299). T.P. and M.X. acknowledge the partial support of their work by the STC Center for Integrated Quantum Materials, National Science Foundation (DMR-1231319).

REFERENCES

(1) Ausfelder, F.; Bazzanella, A. Hydrogen in the Chemical Industry. In *Hydrogen Science and Engineering: Materials, Processes, Systems and Technology*; Stolten, P. D. D., Emonts, D. B., Eds.; John Wiley & Sons: Weinheim, Germany, 2016; pp 19−40.

(2) Johnston, B.; Mayo, M. C.; Khare, A. Hydrogen: The Energy Source for the 21st Century. *Technovation* **2005**, *25*, 569−585.

(3) Qazi, U. Y. Future of Hydrogen as an Alternative Fuel for Next-Generation Industrial Applications; Challenges and Expected Opportunities. *Energies* **2022**, *15*, 4741−4780.

(4) Crabtree, G. W.; Dresselhaus, M. S. The Hydrogen Fuel Alternative. *MRS Bull.* **2008**, *33*, 421−428.

(5) Hübert, T.; Boon-Brett, L.; Black, G.; Banach, U. Hydrogen Sensors - a Review. *Sens. Actuators B Chem.* **2011**, *157*, 329−352.

(6) Zhang, Y.-N.; Peng, H.; Qian, X.; Zhang, Y.; An, G.; Zhao, Y. Recent Advancements in Optical Fiber Hydrogen Sensors. *Sens. Actuators B Chem.* **2017**, *244*, 393−416.

(7) Huang, X. M. H.; Manolidis, M.; Jun, S. C.; Hone, J. Nanomechanical Hydrogen Sensing. *Appl. Phys. Lett.* **2005**, *86*, 143104−143106.

(8) Korotcenkov, G.; Han, S. D.; Stetter, J. R. Review of Electrochemical Hydrogen Sensors. *Chem. Rev.* **2009**, *109*, 1402−1433.

(9) Penner, R. M. A Nose for Hydrogen Gas: Fast, Sensitive H_2 Sensors Using Electrodeposited Nanomaterials. *Acc. Chem. Res.* **2017**, *50*, 1902−1910.

(10) Koo, W.-T.; Cho, H.-J.; Kim, D.-H.; Kim, Y. H.; Shin, H.; Penner, R. M.; Kim, I.-D. Chemiresistive Hydrogen Sensors: Fundamentals, Recent Advances, and Challenges. *ACS Nano* **2020**, *14*, 14284−14322.

(11) Chiu, S.-W.; Tang, K.-T. Towards a Chemiresistive Sensor-Integrated Electronic Nose: A Review. *Sensors* **2013**, *13*, 14214−14247.

(12) Kaniyoor, A.; Ramaprabhu, S. Hybrid Carbon Nanostructured Ensembles as Chemiresistive Hydrogen Gas Sensors. *Carbon* **2011**, *49*, 227−236.

(13) Koo, W.-T.; Jang, J.-S.; Kim, I.-D. Metal-Organic Frameworks for Chemiresistive Sensors. *Chem.* **2019**, *5*, 1938−1963.

(14) Virji, S.; Kaner, R. B.; Weiller, B. H. Hydrogen Sensors Based on Conductivity Changes in Polyaniline Nanofibers. *J. Phys. Chem. B* **2006**, *110*, 22266−22270.

(15) Thathsara, S. K. T.; Harrison, C. J.; Hocking, R. K.; Shafiei, M. Photoactive Semiconducting Metal Oxides: Hydrogen Gas Sensing Mechanisms. *Int. J. Hydrog. Energy* **2022**, *47*, 18208−18227.

(16) Favier, F.; Walter, E. C.; Zach, M. P.; Benter, T.; Penner, R. M. Hydrogen Sensors and Switches from Electrodeposited Palladium Mesowire Arrays. *Science* **2001**, *293*, 2227−2231.

(17) Kim, D.-H.; Kim, S.-J.; Shin, H.; Koo, W.-T.; Jang, J.-S.; Kang, J.-Y.; Jeong, Y. J.; Kim, I.-D. High-Resolution, Fast, and Shape-Conformable Hydrogen Sensor Platform: Polymer Nanofiber Yarn Coupled with Nanograined Pd@Pt. *ACS Nano* **2019**, *13*, 6071−6082.

(18) Gao, M.; Cho, M.; Han, H.-J.; Jung, Y. S.; Park, I. Palladium-Decorated Silicon Nanomesh Fabricated by Nanosphere Lithography for High Performance, Room Temperature Hydrogen Sensing. *Small* **2018**, *14*, 1703691−1703700.

(19) Yang, F.; Kung, S.-C.; Cheng, M.; Hemminger, J. C.; Penner, R. M. Smaller Is Faster and More Sensitive: The Effect of Wire Size on the Detection of Hydrogen by Single Palladium Nanowires. *ACS Nano* **2010**, *4*, 5233−5244.

(20) Zhang, H.; Jin, M.; Xiong, Y.; Lim, B.; Xia, Y. Shape-Controlled Synthesis of Pd Nanocrystals and Their Catalytic Applications. *Acc. Chem. Res.* **2013**, *46*, 1783−1794.

(21) Chen, A.; Ostrom, C. Palladium-Based Nanomaterials: Synthesis and Electrochemical Applications. *Chem. Rev.* **2015**, *115*, 11999−12044.

(22) Watt, J.; Cheong, S.; Tilley, R. D. How to Control the Shape of Metal Nanostructures in Organic Solution Phase Synthesis for Plasmonics and Catalysis. *Nano Today* **2013**, *8*, 198−215.

(23) Rifai, S.; Breen, C. A.; Solis, D. J.; Swager, T. M. Facile in Situ Silver Nanoparticle Formation in Insulating Porous Polymer Matrices. *Chem. Mater.* **2006**, *18*, 21−25.

(24) Koo, W.-T.; Kim, Y.; Savagatrup, S.; Yoon, B.; Jeon, I.; Choi, S.-J.; Kim, I.-D.; Swager, T. M. Porous Ion Exchange Polymer Matrix for Ultrasmall Au Nanoparticle-Decorated Carbon Nanotube Chemiresistors. *Chem. Mater.* **2019**, *31*, 5413−5420.

(25) Koo, W.-T.; Kim, Y.; Kim, S.; Suh, B. L.; Savagatrup, S.; Kim, J.; Lee, S.-J.; Swager, T. M.; Kim, I.-D. Hydrogen Sensors from Composites of Ultra-Small Bimetallic Nanoparticles and Porous Ion-Exchange Polymers. *Chem.* **2020**, *6*, 2746−2758.

(26) Brunel, R.; Marestin, C.; Martin, V.; Mercier, R.; Schiets, F. Assisted Microwave Synthesis of High Molecular Weight Poly(Aryletherketone) s. *High Perform. Polym.* **2008**, *20*, 185−207.

(27) Schroeder, V.; Savagatrup, S.; He, M.; Lin, S.; Swager, T. M. Carbon Nanotube Chemical Sensors. *Chem. Rev.* **2019**, *119*, 599−663.

(28) Kauffman, D. R.; Star, A. Carbon Nanotube Gas and Vapor Sensors. *Angew. Chem., Int. Ed.* **2008**, *47*, 6550−6570.

(29) Zaporotskova, I. V.; Boroznina, N. P.; Parkhomenko, Y. N.; Kozhitov, L. V. Carbon Nanotubes: Sensor Properties. A Review. *Mod. Electron. Mater.* **2016**, *2*, 95−105.

(30) Wang, Y.; Yeow, J. T. W. A Review of Carbon Nanotubes-Based Gas Sensors. *J. Sens.* **2009**, *2009*, 493904−493927.

(31) Tsui, N. T.; Paraskos, A. J.; Torun, L.; Swager, T. M.; Thomas, E. L. Minimization of Internal Molecular Free Volume: A Mechanism for the Simultaneous Enhancement of Polymer Stiffness, Strength, and Ductility. *Macromolecules* **2006**, *39*, 3350−3358.

(32) Favier, I.; Pla, D.; Gómez, M. Palladium Nanoparticles in Polyols: Synthesis, Catalytic Couplings, and Hydrogenations. *Chem. Rev.* **2020**, *120*, 1146−1183.

(33) Shen, Y.; Yamazaki, T.; Liu, Z.; Meng, D.; Kikuta, T.; Nakatani, N.; Saito, M.; Mori, M. Microstructure and H_2 Gas Sensing Properties of Undoped and Pd-Doped SnO_2 Nanowires. *Sens. Actuators B Chem.* **2009**, *135*, 524−529.

(34) Meng, D.; Yamazaki, T.; Kikuta, T. Preparation and Gas Sensing Properties of Undoped and Pd-Doped TiO_2 Nanowires. *Sens. Actuators B Chem.* **2014**, *190*, 838−843.

(35) Chiang, Y.-J.; Li, K.-C.; Lin, Y.-C.; Pan, F.-M. A Mechanistic Study of Hydrogen Gas Sensing by PdO Nanoflake Thin Films at Temperatures Below 250 °C. *Phys. Chem. Chem. Phys.* **2015**, *17*, 3039−3049.

(36) Brun, M.; Berthet, A.; Bertolini, J. C. XPS, AES and Auger Parameter of Pd and PdO. *J. Electron Spectrosc. Relat. Phenom.* **1999**, *104*, 55−60.

(37) Kim, K. S.; Gossmann, A. F.; Winograd, N. X-Ray Photoelectron Spectroscopic Studies of Palladium Oxides and the Palladium-Oxygen Electrode. *Anal. Chem.* **1974**, *46*, 197−200.

(38) Zhan, B.; Li, C.; Yang, J.; Jenkins, G.; Huang, W.; Dong, X. Graphene Field-Effect Transistor and Its Application for Electronic Sensing. *Small* **2014**, *10*, 4042−4065.

(39) Fu, W.; Jiang, L.; van Geest, E. P.; Lima, L. M. C.; Schneider, G. F. Sensing at the Surface of Graphene Field-Effect Transistors. *Adv. Mater.* **2017**, *29*, 1603610.

(40) Ohno, Y.; Maehashi, K.; Matsumoto, K. Chemical and Biological Sensing Applications Based on Graphene Field-Effect Transistors. *Biosens. Bioelectron.* **2010**, *26*, 1727−1730.

(41) Stine, R.; Mulvaney, S. P.; Robinson, J. T.; Tamanaha, C. R.; Sheehan, P. E. Fabrication, Optimization, and Use of Graphene Field Effect Sensors. *Anal. Chem.* **2013**, *85*, 509−521.

(42) Xue, M.; Mackin, C.; Weng, W.-H.; Zhu, J.; Luo, Y.; Luo, S.-X. L.; Lu, A.-Y.; Hempel, M.; McVay, E.; Kong, J.; Palacios, T. Integrated Biosensor Platform Based on Graphene Transistor Arrays for Real-Time High-Accuracy Ion Sensing. *Nat. Commun.* **2022**, *13*, 5064−5074.

(43) Ishihara, S.; O'Kelly, C. J.; Tanaka, T.; Kataura, H.; Labuta, J.; Shingaya, Y.; Nakayama, T.; Ohsawa, T.; Nakanishi, T.; Swager, T. M. Metallic Versus Semiconducting Swcnt Chemiresistors: A Case for Separated SWCNTs Wrapped by a Metallosupramolecular Polymer. *ACS Appl. Mater. Interfaces* **2017**, *9*, 38062−38067.

(44) Luo, S.-X. L.; Lin, C.-J.; Ku, K. H.; Yoshinaga, K.; Swager, T. M. Pentiptycene Polymer/Single-Walled Carbon Nanotube Complexes: Applications in Benzene, Toluene, and *o*-Xylene Detection. *ACS Nano* **2020**, *14*, 7297−7307.

(45) Jorio, A.; Pimenta, M. A.; Filho, A. G. S.; Saito, R.; Dresselhaus, G.; Dresselhaus, M. S. Characterizing Carbon Nanotube Samples with Resonance Raman Scattering. *New J. Phys.* **2003**, *5*, 139−139.

(46) You, H.; Fu, C.; Wang, M.; Yang, C.; Shi, Y.; Pan, H.; Lin, Q. Pd/CNT with Controllable Pd Particle Size and Hydrophilicity for Improved Direct Synthesis Efficiency of H_2O_2. *New J. Chem.* **2022**, *46*, 12093−12102.

(47) Robinson, J. A.; Snow, E. S.; Bădescu, Ş. C.; Reinecke, T. L.; Perkins, F. K. Role of Defects in Single-Walled Carbon Nanotube Chemical Sensors. *Nano Lett.* **2006**, *6*, 1747−1751.

(48) *Multi-Year Research, Development, and Demonstration Plan, 576 2011−2020. Section 3.7 Hydrogen Safety, Codes and Standards*; Energy Efficiency and Renewable Energy (EERE), Department of Energy: Washington, DC, 2015.

(49) Abdulhamid, M. A.; Park, S.-H.; Vovusha, H.; Akhtar, F. H.; Ng, K. C.; Schwingenschlögl, U.; Szekely, G. Molecular Engineering of High-Performance Nanofiltration Membranes from Intrinsically Microporous Poly(Ether-Ether-Ketone). *J. Mater. Chem. A* **2020**, *8*, 24445−24454.

(50) Pournaghshband Isfahani, A.; Sadeghi, M.; Wakimoto, K.; Shrestha, B. B.; Bagheri, R.; Sivaniah, E.; Ghalei, B. Pentiptycene-Based Polyurethane with Enhanced Mechanical Properties and CO_2-Plasticization Resistance for Thin Film Gas Separation Membranes. *ACS Appl. Mater. Interfaces* **2018**, *10*, 17366−17374.